Impact of spray dynamics on combustion instabilities investigated by changing the atomizer recess in a swirl combustor

Preethi Rajendram Soundararajan, D. Durox, Antoine Renaud, Sébastien Candel

To cite this version:

Preethi Rajendram Soundararajan, D. Durox, Antoine Renaud, Sébastien Candel. Impact of spray dynamics on combustion instabilities investigated by changing the atomizer recess in a swirl combustor. Combustion and Flame, 2023, 252, pp.112757. ⟨10.1016/j.combustflame.2023.112757⟩. ⟨hal-04097959⟩

HAL Id: hal-04097959

https://centralesupelec.hal.science/hal-04097959v1

Submitted on 15 May 2023

Impact of spray dynamics on combustion instabilities investigated by changing the atomizer recess in a swirl combustor [*]

Preethi Rajendram Soundararajan[†a], Daniel Durox[a], Antoine Renaud[a], Sébastien Candel[a]

[a]Laboratoire EM2C, CNRS, CentraleSupélec, Université Paris-Saclay, 3 rue Joliot Curie, 91190 Gif-sur-Yvette, France

---

Abstract

The present article is aimed at identifying the impact of spray dynamics on combustion instabilities. This is achieved by systematically modifying the liquid fuel atomizer location with respect to the injector outlet in experiments carried out on a single-injector swirling combustor. The injector is characterized by a high swirl number and a relatively high pressure drop, and features a pressure atomizer that delivers liquid heptane fuel in the form of a fine spray. In the first set of experiments, longitudinal self-sustained oscillations (SSOs) are examined by varying the atomizer recess distance and using three combustion chamber lengths. Three distinct instability regions characterized by jumps in amplitude and frequency are observed as a function of the atomizer recess. At lower SSO frequencies (obtained for longer chambers), the pressure fluctuation amplitude in the chamber decreases as the atomizer recess distance is reduced, tending towards a stable operation. An opposite behavior is observed at comparatively higher SSO frequencies (obtained with a shorter chamber), where the system becomes less unstable at higher atomizer recess distances. The oscillation frequency is also found to change and increases as the recess distance is reduced. Three recess distances corresponding to each zone of operation are selected to further analyze the flow and flame structures and dynamics. It is found that the mean velocity profiles only reveal moderate differences in the air flow field, but there are significant changes in the fuel spray distribution in the neighborhood of the injector axis. Laser sheet images of the spray reveal two patterns—one where the spray predominantly interacts with the injector end piece when the atomizer is recessed, and the other where this interaction is minimal. In the latter case, corresponding to a small recess, the fuel spray is directly conveyed into the chamber. It is next found that the spray distribution affects the flame pattern defining two distinct configurations. Finally, the flame response to external disturbances is characterized by flame describing functions (FDFs) that allow carrying out a stability analysis. FDF results obtained with two independent methods indicate that the gain and phase at the three recess positions vary substantially and that this can be used in combination with a low-order model to interpret the instability behavior of the system. This study might serve to guide the modeling of combustion dynamics and help design injectors that are less sensitive to instabilities.

Keywords: Thermoacoustic instabilities, Flame describing function, Swirl combustor, Pressure-swirl atomizer, Passive instability control

---

1. Introduction

Combustion instabilities characterized by high-amplitude pressure fluctuations are extensively investigated because of their detrimental effects [1–3]. The case of liquid fuels is of particular interest to the aviation industry, and several studies on combustion instabilities in lab-scale annular combustors specifically operated with liquid spray flames [4, 5] as well as studies on real annular combustors [6] have provided some valuable insights. Injection of liquid fuel in the form of a spray adds complexity to the mechanism leading to these instabilities as time lags associated with vaporization and mixing may alter the stability domains of the combustors [7–11]. In this context, the present article describes experiments aimed at identifying effects of spray dynamics on combustion instabilities. This

---

[*] Published version DOI: https://doi.org/10.1016/j.combustflame.2023.112757

[†] Corresponding author: Preethi Rajendram Soundararajan. *Email address*: pr516@cam.ac.uk

Present address: Department of Engineering, University of Cambridge, Cambridge, England CB2 1PZ, United Kingdom.

is accomplished by changing the location of the spray atomizer with respect to the injector outlet, examining the dynamical characteristics corresponding to these changes and interpreting these features by considering the flow and flame structures, measuring the flame describing functions (FDFs) and using these FDFs in a stability analysis of the system.

At this stage, it is worth reviewing some previous works that specifically investigated the effect of spray dynamics on instabilities. The case of a cold spray ensuing from an air-blast atomizer and subjected to acoustic modulation was studied in [12]. Fluctuations in the spray number density and droplet size distribution were observed that could lead to the formation of hot spots under reactive conditions, constituting a potential source of combustion instability. Other experimental and numerical studies under cold flow conditions also confirmed the dependence of droplet size distribution [13], spray structure [14], and evaporation rate [15] on the frequency and amplitude of incident acoustic disturbances. A direct numerical simulation of an externally modulated bunsen spray flame in [16] showed that for droplets with a significant Stokes number, the flame response was additionally affected by mixture fraction variations caused by preferential droplet segregation. Such droplet number densifications were also reported in [17] in an oscillatory flow field, leading to flame front pinching and a subsequent flame shape transformation. The effect of convective time delay associated with droplets on self-sustained instabilities was identified in [18] on a swirl combustor equipped with an air-blast atomizer. The oscillation frequency, in this case, was found to be mainly dictated by the convection time of fuel from the atomizer lip to the flame zone. Apeloig et al. [19] showed that the convective time scales of the spray could be modified by wall interactions. It was found that during some parts of the acoustic cycle, the liquid droplet stream interacted with the swirler walls, forming a liquid film, which was further convected and subsequently re-atomized by the air flow, while at other instants of the cycle, the droplets rebounded or were transported directly into the chamber from their injection point. The impact of spray-wall interaction on thermoacoustic instabilities was also emphasized in [20] through large eddy simulations (LES) of the SICCA-Spray combustor of the EM2C laboratory equipped with an injector similar to those considered in the present investigation. The authors found that a slip boundary condition on the walls of the exit nozzle did not reproduce the experimental observations. Whereas, by considering a film boundary condition on the wall and modeling the subsequent formation and atomization of the liquid film, they reproduce the limit cycle observed experimentally. Several other studies (see, for example, [21–24]) have also identified the effect of spray-flame coupling mechanisms, motivating further investigations in this domain. In a recent study by Lo Schiavo et al. [25], the impact of spray injection angle was considered through the LES of the SICCA-Spray combustor. Even though the influence of spray angle on the stable flame shape was negligible, it completely altered the instability behavior—the system tended to become stable when the spray angle was diminished. Using numerical modeling, it was shown that this variation of spray angle affected the interaction of spray with the walls of the exit nozzle, modifying the liquid film-acoustic coupling. Experimentally, with a given atomizer it is not possible to change the spray angle, but it is easy to change the fuel atomizer location, thus altering the recess distance from the combustor backplane. It is known from liquid rocket engine applications that this distance influences the flame structure and dynamics of coaxial injectors, as shown, for example, in [26]. The flame expansion rate is notably augmented if the central channel conveying liquid oxygen is in recess with respect to the outlet. This is because the confined central stream becomes absolutely unstable, which possibly enhances the mixing and spreading rate. Recent LES of swirling coaxial liquid rocket injectors [27] indicate that pressure oscillations arise when the recess distance takes the largest value. Another recent LES study [28] with similar injectors as [27] confirms that the recess influences the flame shape and the injector head loss. The previous review indicates that it may be interesting to change the atomizer recess distance in a swirl spray injector, as will be done in the present study, to see how the spray influences the combustion dynamics and the processes leading to instabilities. The corresponding data and understanding may eventually help design injectors that are less susceptible to instabilities and develop control strategies for instability mitigation.

One such strategy was proposed in [29] on a technically premixed can combustor, where experiments were carried out to study the effect of moving the fuel injection location along the axis of the premix nozzle. The instability regimes (both in amplitude and frequency) were found to depend on the fuel injection position, which was subsequently explained using a time lag model. By moving the fuel injection location, the distance and correspondingly the time taken for the air-fuel mixture to reach the flame front was changed for a given nozzle velocity, thus affecting the phase between heat release rate and pressure. Although a stable operation of the combustor could not be achieved by simply changing the fuel injection location in this study, it was possible to obtain a stable operating regime by injecting the fuel from two axial fuel ports. In [30], a slow active control method of damping instabilities based on varying the

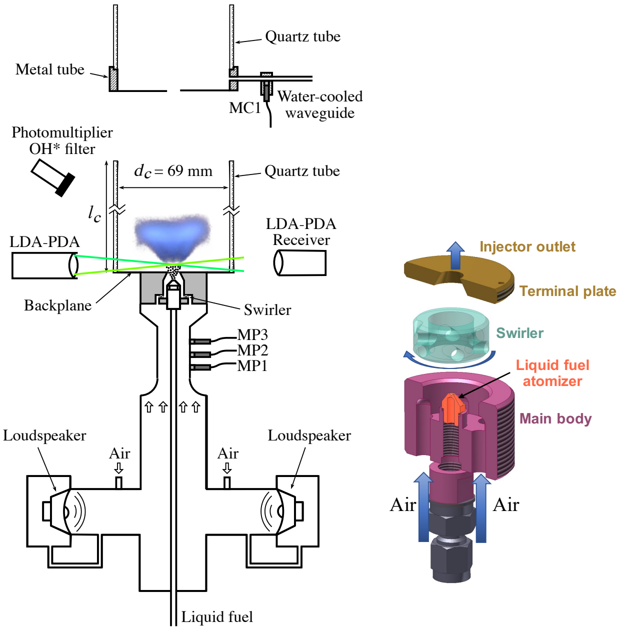

(a) (b)

Figure 1: (a) Experimental setup of the SICCA-Spray test rig. (b) Exploded view of the injector unit adapted from [31].

fuel spray properties using a Nanomizer$^{\text{TM}}$ unit was successfully demonstrated. By varying the power input to the fuel injector, it was possible to change the droplet diameters, which resulted in modified stability behaviors. The above studies thus indicate a possibility of developing control techniques by altering the fuel injection location and, consequently, the fuel spray characteristics.

This is attempted in the present study by modifying the fuel atomizer position with the aim of developing deeper insights into the influence of spray dynamics on instabilities. As will be seen later, unlike in the study of [30], the droplet distribution remains nearly the same in the present study, but the spray-wall interaction mechanism is altered, leading to different convective time scales and spatial dispersion of the spray when the fuel atomizer position is varied.

This article is organized as follows. After a presentation of the experimental setup (Section 2), Section 3 describes the self-sustained instabilities obtained by systematically varying the fuel atomizer position. The spray and flame patterns are then analyzed, and the observed regimes of self-sustained oscillations are interpreted by using the measured FDFs (in Sections 4 and 5, respectively).

2. Experimental setup

2.1. SICCA-Spray test rig

Experiments are carried out in the SICCA-Spray combustor, which represents a single sector of the MICCA-Spray annular combustor mainly used to investigate azimuthal instabilities and light round ignition processes [11, 32]. The experimental setup, shown in Fig. 1 (a), comprises a swirling injector that connects the plenum to the combustion chamber. Air from the plenum passes through the six tangential channels of the swirler, inducing a clockwise rotation of the air stream. The air flow rate is controlled by a *Bronkhorst* EL-FLOW$^{\circledR}$ mass flow meter with a full range of $150\,\mathrm{L_n/min}$ and relative accuracy of 0.6%. The injector used in this study has a high pressure drop of $6\,\mathrm{kPa}$ and abrupt area changes in the swirler channels making it only weakly transparent to acoustic waves. Liquid heptane, used as fuel, is delivered by a pressure atomizer having an orifice diameter of $80\,\mu\mathrm{m}$. The atomizer is threaded onto the injector such that its position can be continuously varied along the injector axis. Fuel is delivered via a central tube passing through the plenum and feeds the atomizer that establishes a hollow-cone spray of droplets. The swirling air surrounding the atomizer assists in opening up the liquid spray cone and aids in breaking up the fuel jet. The fuel flow rate is controlled by a *Bronkhorst* CORI-FLOW® with a full range of $1\,\mathrm{kg\,h^{-1}}$ and a relative accuracy of 0.2%. The injector houses a terminal plate with an exit diameter of $8\,\mathrm{mm}$. This component features a $5\,\mathrm{mm}$-long conical section followed by a $1\,\mathrm{mm}$-long cylindrical section. The swirler, fuel atomizer, and terminal plate compose the injector shown in Fig. 1 (b). In the present experiments, the test rig is operated at a thermal power of $\mathcal{P}_{\mathrm{th}} = 6.4\,\mathrm{kW}$ and global equivalence ratio of $\phi = 0.85$. This corresponds to an air flow rate of $\dot{m}_a = 120\,\mathrm{L_n/min}$ and a fuel flow rate of $\dot{m}_f = 520\,\mathrm{g\,h^{-1}}$.

The modular construction of the SICCA-Spray test rig allows performing two kinds of experiments. In the first set, the combustion chamber length is varied to produce longitudinal self-sustained oscillations (SSOs) of different frequencies and amplitudes. Three chamber lengths are used in the present study, $l_c = 215\,\mathrm{mm}$, $265\,\mathrm{mm}$ and $365\,\mathrm{mm}$, all with an inner diameter of $d_c = 69\,\mathrm{mm}$. At each chamber length, the atomizer position is varied continuously to identify the effect of atomizer location on SSOs exhibited by the combustor. In the second set of experiments, the two driver units (*Monacor* SP-6/108PRO hi-fi loudspeakers) mounted at the bottom of the plenum modulate the system at different frequencies and amplitudes to obtain the FDFs. During these experiments, the chamber length is fixed and equal to $l_c = 150\,\mathrm{mm}$ to avoid SSOs and ensure the flame is stable [33]. A wave generator connected to the driver units produces frequency ramps between $250\,\mathrm{Hz}$ and $850\,\mathrm{Hz}$ at the rate of $4.5\,\mathrm{Hz\,s^{-1}}$ at six amplifier voltages to produce different velocity fluctuation levels $u'_{c,r}/\overline{u}_{c,r}$ at the base of the flame. The driver units do not operate and are left electrically open during the first set of experiments while obtaining the SSO characteristics.

2.2. Diagnostic tools

The test rig is equipped with different diagnostic tools that are primarily used to measure the velocity, pressure and light intensity fluctuations. The pressure signal in the combustion chamber is recorded by a microphone MC1 (Fig. 1 (a) top) plugged onto a water-cooled waveguide. The waveguide is connected via a brass ring of $69\,\mathrm{mm}$ diameter and $15\,\mathrm{mm}$ length mounted on the backplane. The microphone located at a distance of $276\,\mathrm{mm}$ from the waveguide port is protected from the high-temperature environment in the chamber. But this introduces a propagation delay of $0.79\,\mathrm{ms}$ in the measured acoustic pressure, which is accounted for in the data processing. Three other microphones mounted on waveguides are plugged onto a metal hat and placed on the downstream side of the flame at a distance of 110, 125 and $140\,\mathrm{mm}$ from the chamber backplane. This arrangement (schematically shown in Fig. A.9), in addition to obtaining the pressure fluctuations, allows measuring the acoustic velocity downstream of the flame by the multi-microphone method [34]. The remainder of the chamber is formed by a quartz tube providing the optical access needed for recording the chemiluminescence $I(OH^*)$ from the flame. This is measured by a *Thorn EMI Electron Tubes* photomultiplier fitted with an OH* filter centered at $308\,\mathrm{nm}$. A *Dantec Dynamics* 2-component phase Doppler particle analyzer (PDPA) system provides the velocity of heptane droplets. These measurements are mainly performed to obtain axial velocity profiles at the injector outlet while operating under laser Doppler anemometry (LDA) mode to ensure the maximum possible data rate. Axial, radial and tangential velocity profiles are only determined under cold flow conditions by seeding the air flow with fine oil droplets having a mean diameter of $2.5\,\mathrm{\mu m}$ and discussed in Section 4.1. More details on LDA measurements are given in [35]. The particle size distributions discussed in Section 4.3 are obtained by operating the PDPA system in the phase Doppler anemometry (PDA) mode. An intensified camera equipped with a UV lens and an OH* filter centered at $308\,\mathrm{nm}$ is used to obtain the flame images. Laser light sheet scattering images are used to characterize the spray. These images are recorded by removing the chamber confinement to avoid parasitic reflections. The light sheet is formed by a continuous Nd:YAG laser with a wavelength of $532\,\mathrm{nm}$.

3. Regimes of self-sustained oscillations (SSOs)

Pressure fluctuations are measured in SICCA-Spray for three chamber lengths $l_c = 365\,\mathrm{mm}$, $265\,\mathrm{mm}$, and $215\,\mathrm{mm}$, and at each length, the atomizer position is systematically varied. The atomizer recess h_r refers to the distance of this unit with respect to the chamber backplane. The atomizer is moved continuously from $h_r = 9.25\,\mathrm{mm}$ (lowest position) to $1.75\,\mathrm{mm}$ (highest position) in steps of $0.5\,\mathrm{mm}$ to obtain the instability characteristics at sixteen recess distances. At each position, the microphone MC1 measures the acoustic pressure level in the chamber, and the signals are sampled at a rate of 16,384 Hz for an acquisition time of at least $10\,\mathrm{s}$. Measurements are performed when

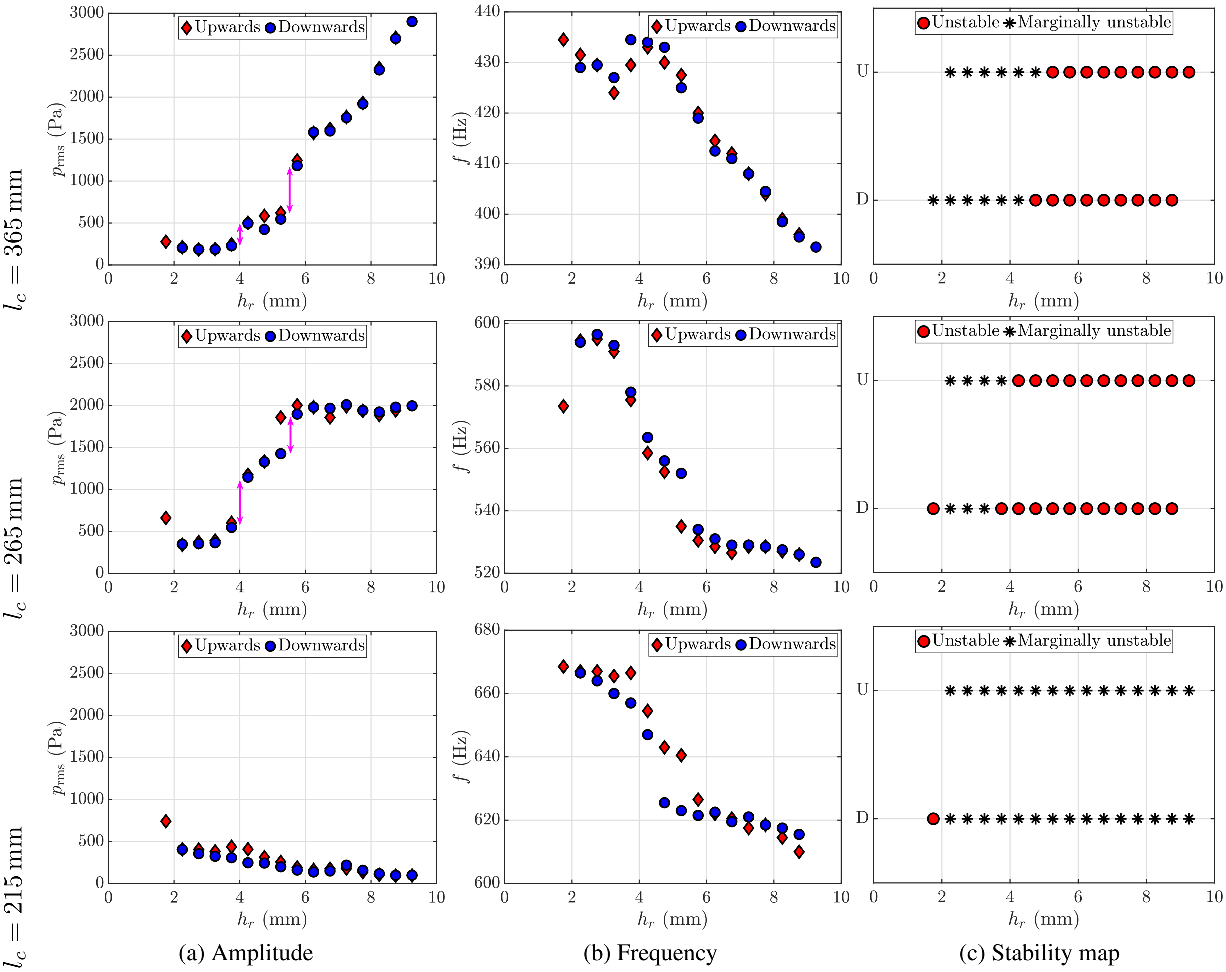

(a) Amplitude (b) Frequency (c) Stability map

Figure 2: Amplitude (a) and frequency (b) of SSO at three chamber lengths $365\,\mathrm{mm}$, $265\,\mathrm{mm}$ and $215\,\mathrm{mm}$ and for different recess distances. The vertical arrows in (a) at $365\,\mathrm{mm}$ and $265\,\mathrm{mm}$ point to the jumps corresponding to changes in the system's state. (c) Stability map at different recess distances. U: Upwards; D: Downwards.

the atomizer is moved upwards as well as downwards to see if there is any hysteresis effect. The recess distance is not reduced below $1.75\,\mathrm{mm}$ to avoid flame stabilization on the atomizer head, which would eventually damage this unit.

Figure 2 (a) and (b) show the amplitude and frequency of SSO at different atomizer recess distances both for downward (increasing the recess distance) as well as upward (decreasing the recess distance) movements. The frequency of oscillation is obtained by determining the peak frequency of the power spectrum, and the root mean square (RMS) pressure amplitude is calculated as the square root of the integrated power spectral density multiplied by the frequency resolution Δf.

At $l_c = 365\,\mathrm{mm}$ and $265\,\mathrm{mm}$, a general tendency of increased amplitude and decreased frequency can be observed as the recess distance h_r is augmented. From the amplitude map, one distinguishes two jumps (represented by vertical arrows), resulting in three well-defined regions of operation. Each jump could be envisaged as a change in the state of the fuel injection geometry leading to a change in the system behavior. For both chamber lengths, one identifies three zones, the first between $1.75\,\mathrm{mm}$ and $3.75\,\mathrm{mm}$, the second between $4.25\,\mathrm{mm}$ and $5.25\,\mathrm{mm}$, and the final one between $5.75\,\mathrm{mm}$ and $9.25\,\mathrm{mm}$. Amplitude jumps are accompanied by frequency jumps, but this is less apparent in the $l_c = 365\,\mathrm{mm}$ case. No visible hysteresis is seen between the two operations as the system follows the same trajectory between downwards and upwards motion, with minor differences existing at the jump locations. The tendency after these jumps is not necessarily the same between the two chamber lengths. At $l_c = 265\,\mathrm{mm}$, the amplitude in each zone appears to reach a plateau, whereas the frequency shows a continuous decrease. For $l_c = 365\,\mathrm{mm}$, the first two jumps result in the plateauing of the amplitude, whereas after the final jump, the amplitude does not plateau but keeps increasing. The frequency monotonically decreases in the first and third zones, whereas it remains nearly constant in the second zone. Although with each increase in recess distance, the system has a slightly higher pressure amplitude, at $265\,\mathrm{mm}$, the plateauing of amplitude in the final zone results in a smaller amplitude at the largest recess distance compared to $365\,\mathrm{mm}$, which has a higher amplitude at this state.

On the other hand, the instability tendency at $l_c = 215\,\mathrm{mm}$ (third row of Fig. 2) differs from that found for the other two chamber lengths. The amplitude is much smaller and exhibits a reverse trend compared to the other two lengths, i.e., the instability amplitude is diminished when the recess distance is increased, and the RMS pressure tends to zero at higher recess distances, as seen from the third row of Fig. 2 (a). Unlike the other two cases, no distinct jumps are observed in the amplitude stability map, and the variation occurs gradually with changes in the recess distance. This is probably because the system is already close to its stability limit and any change caused by modifying the recess distance is not sufficient to alter the system's stability domain. The frequency map shows a similar tendency as the other two chamber lengths and decreases when the atomizer recess distance is increased with a jump occurring at $h_r = 4.75\,\mathrm{mm}$.

The stability map, shown in Fig. 2 (c), relies on a stability criterion introduced in [35], where the system is compared to a stable baseline configuration with $l_c = 115\,\mathrm{mm}$ to classify the unstable regimes. Two metrics are determined: one related to RMS pressure amplitude and the other to peak prominence in the power spectrum. When only one of these two criteria is met, the system is deemed marginally unstable. The system is seen to move from a highly unstable operation (indicated by circles) to a marginal instability (indicated by stars) as the atomizer recess distance h_r is diminished at $l_c = 365$ and $265\,\mathrm{mm}$, and the recess distance at which this transition occurs is nearly the same for the two chamber lengths. At the smallest recess distance, p_{rms} is relatively low, indicating that the system is approximately stable. At $l_c = 215\,\mathrm{mm}$, the instability is only marginal at all the recess distances except when the atomizer is at its closest position to the backplane, where the system becomes unstable.

To further understand the system behavior in each instability zone, three recess distances are selected at $h_r = 2.75\,\mathrm{mm}$, $4.75\,\mathrm{mm}$, and $6.75\,\mathrm{mm}$, corresponding to each zone. As will be seen later, the extent of spray-wall interaction at each of these locations changes, leading to a modified instability behavior of SICCA-Spray. Detailed measurements at these selected locations are presented in the following sections.

4. Measurements under stable conditions

It is instructive to successively examine velocity profiles under cold flow conditions, spray configurations under cold and unconfined conditions using laser light scattering, droplet size distributions in the liquid spray under hot fire conditions and flame images corresponding to the three chosen atomizer locations. These data are obtained under stable operating conditions.

4.1. Velocity profiles under cold flow conditions

Velocity profiles are measured with the PDPA system under cold flow conditions with a chamber length of $l_c = 150\,\mathrm{mm}$. The air flow is seeded with fine oil droplets ($d_{10} \approx 2.5\,\mu\mathrm{m}$) to obtain three velocity components at different radii and at a height of $2.5\,\mathrm{mm}$ above the backplane. Figure 3 shows the mean and RMS profiles for axial (u_x), radial (u_r), and tangential (u_θ) velocity components. The mean velocity profiles are similar for the three recess distances except for minor differences in the peak level of axial and radial components. Contrary to the mean profile, the RMS velocity profiles reveal two distinct categories: one corresponding to $6.75\,\mathrm{mm}$ and the second family belonging to the two smaller recess distances.

The swirl number can be deduced from the measured mean velocity profiles using an integration as explained in [36]. This is given by:

$$S_N = \frac{\int_0^{2R_{\text{inj}}} \overline{u}_\theta \overline{u}_x r^2 dr}{R_{\text{inj}} \int_0^{2R_{\text{inj}}} \overline{u}_x^2 r dr} \tag{1}$$

where $R_{\text{inj}} = 4\,\mathrm{mm}$ is the radius at the injector outlet. The values calculated using the above expression are $S_N = 0.77$ for $h_r = 2.75\,\mathrm{mm}$, $S_N = 0.75$ for $h_r = 4.75\,\mathrm{mm}$, and $S_N = 0.72$ for $h_r = 6.75\,\mathrm{mm}$. At $h_r = 6.75\,\mathrm{mm}$, the atomizer

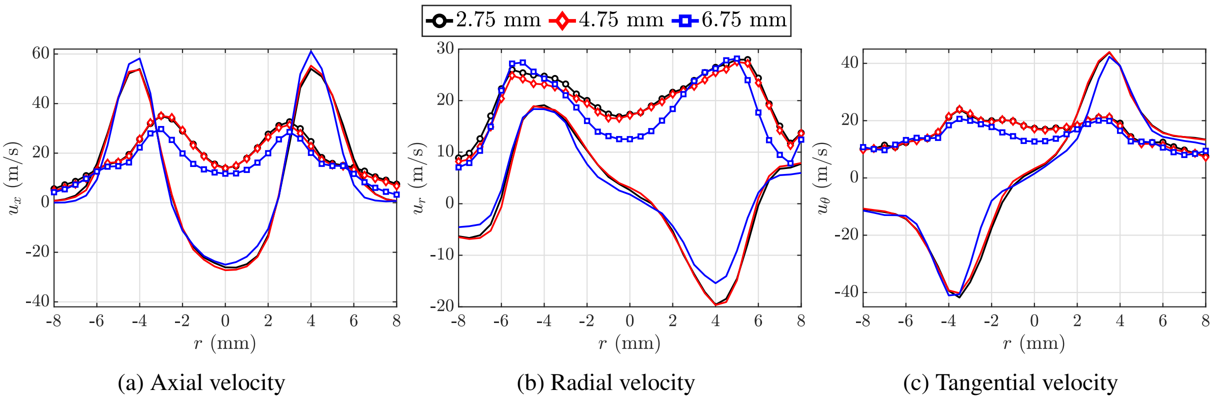

(a) Axial velocity (b) Radial velocity (c) Tangential velocity

Figure 3: Velocity profiles of the air flow at different radii showing the evolution of the mean (solid line without marker) and RMS (solid line with marker) axial (u_x), tangential (u_θ), and radial (u_r) velocity components at three different recess distances. The measurements are made at 2.5 mm above the backplane with the quartz tube confinement under cold flow conditions with oil seeding.

is slightly below the swirler level, but when the recess distance is further decreased, the atomizer is located in the path of the swirling air flow, inducing a minor variation in swirl number. Although minor differences exist, the velocity profiles reveal no marked changes that might explain the observed behavior at the various recess distances. It is next worth exploring the spray behavior, which is discussed in the following sections.

4.2. *Spray tomographic images*

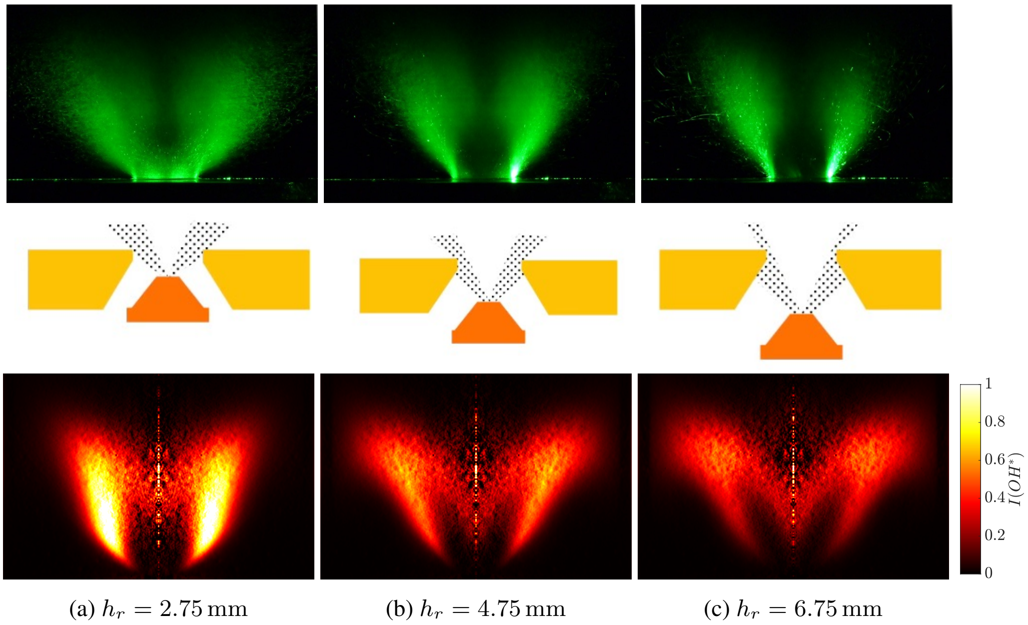

(a) $h_r = 2.75\,\mathrm{mm}$ (b) $h_r = 4.75\,\mathrm{mm}$ (c) $h_r = 6.75\,\mathrm{mm}$

Figure 4: Top: Spray tomographic images at three atomizer positions obtained by illuminating the liquid spray with a laser light sheet. Middle: Schematic showing mean spray evolution at the three atomizer positions. Bottom: Flame images showing OH* chemiluminescence obtained under steady conditions. An Abel deconvolution algorithm is applied to the images captured by the camera and displayed in false colors.

The spray images shown in Fig. 4 (top row) are obtained under cold flow conditions without chamber confinement. A mean spray angle is determined by placing the atomizer almost at level with the backplane; this angle is then used to schematically plot the spray trajectories as shown in Fig. 4 (middle row) at the different atomizer positions. It is interesting to note that the spray angle is much smaller without the surrounding swirl, and the swirling air helps open the hollow cone spray [37]. At $h_r = 2.75\,\mathrm{mm}$, the laser sheet scattering images reveal the presence of droplets throughout the region above the backplane. This is not the case for $h_r = 4.75\,\mathrm{mm}$ and $6.75\,\mathrm{mm}$, where droplets are essentially absent in the central region around the injector axis. This indicates that there are two regions in the spray: one close to the axis, where the droplets are directly issued from the atomizer, as shown in Fig. 4 (middle row, (a)), and a second one close to the edge of the injector outlet, where the fuel spray is formed after interaction with the conical section of the terminal plate as shown in Fig. 4 (middle row, (b) & (c)). At $h_r = 2.75\,\mathrm{mm}$, the spray directly exits into the chamber with only a small portion impacting the conical end piece. When $h_r = 4.75\,\mathrm{mm}$, the spray is displaced towards the injector periphery with only a small amount of droplets remaining in the central region. At $h_r = 6.75\,\mathrm{mm}$, most of the spray originates from the injector edge. When the atomizer recess is increased, most of the initial spray hits the conical wall and enters into the chamber along the injector edge. Two possibilities could be envisaged when such a spray-wall interaction takes place. In the first scenario, the spray particles hitting the wall may form a liquid film that undergoes secondary atomization due to the shearing action of the inner air flow on one side and recirculating gases near the chamber backplane on the other side, producing small droplets that are convected away by the flow. A recent LES of a similar injector [25] reproduces this behavior when the fuel injection angle is varied. It was shown that when the injection angle was augmented, spray-wall interactions led to the formation of a film, and this film was susceptible to acoustic coupling giving rise to instability under certain conditions. It was also found that when the spray angle was diminished, the spray was directly conveyed into the chamber and the level of instability was reduced, in fact, matching some of the experimental observations reported in Section 3 of this article. However, as will be seen in the next section, the droplet diameter distribution remains nearly the same at the injector exit at all three recess positions of the atomizer, which might not be the case if a liquid film undergoing subsequent atomization were present. The other possible outcome of spray-wall interaction might simply be that the particles hitting the wall are bouncing back or sliding along the conical wall and then being swept away by the air flow. One cannot be sure of the exact mechanism, but whatever that may be, it is clear from the spray tomographic images in Fig. 4 (top row) that the spatial extent of the spray and possibly the convection time for any specific fuel droplet are modified. The laser sheet scattering images also indicate that the spray envelope spans a broad region when $h_r = 2.75\,\mathrm{mm}$, whereas it narrows down as the recess is increased (Fig. 4 top row).

4.3. *Liquid droplet counts and size distributions*

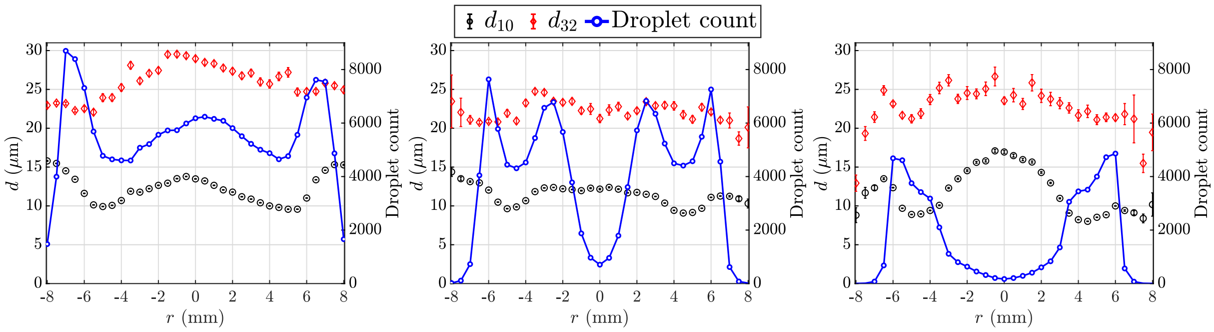

(a) $h_r = 2.75\,\mathrm{mm}$ (b) $h_r = 4.75\,\mathrm{mm}$ (c) $h_r = 6.75\,\mathrm{mm}$

Figure 5: Granulometry profiles of the liquid spray showing mean diameter (d_{10}) and Sauter mean diameter (d_{32}) measured at different radii and three recess distances. The droplet count acquired by the PDPA system at each radial position is plotted in blue circles. The measurements are made at a height of $2.5\,\mathrm{mm}$ above the backplane.

It is also instructive to examine the droplet size profiles under hot fire conditions plotted in terms of mean diameter (d_{10}) and Sauter mean diameter (d_{32}), as shown in Fig. 5 for the three recess values. Size distribution profiles and droplet counts in the spray are measured using PDA at a distance of $2.5\,\mathrm{mm}$ above the backplane. The d_{32} distributions are quite similar, except for $h_r = 2.75\,\mathrm{mm}$, where the spray features comparatively larger d_{32} values in the central region. The droplet counts confirm that the droplets are present in a broad region when h_r is small (Fig. 5(a)), but the droplets are evacuated from the central region when h_r is augmented (Fig. 5(b)) and essentially absent when h_r takes its largest value (Fig. 5(c)). The diameter d_{10} remains nearly the same (around $10\,\mu\mathrm{m}$) at the three atomizer positions close to the injector outlet radius ($R_{\text{inj}} = 4\,\mathrm{mm}$). The size is comparatively larger near the injector center at $6.75\,\mathrm{mm}$, but the droplet count is too low to infer this substantially.

4.4. *Steady state flame images*

The OH* chemiluminescence images of the flame under steady conditions are displayed in Fig. 4 (bottom row). These images are obtained by accumulating 35 frames and applying an Abel deconvolution algorithm. The flame images corresponding to the various atomizer recess distances show noticeable differences and can be primarily distinguished by three factors: overall flame shape, the appearance of the side branches, and light intensity. At the smallest recess distance $h_r = 2.75\,\mathrm{mm}$, the flame takes a relatively narrow-"M" shape. The flame is characterized by broad upright side branches that are luminous. When the recess distance is increased, the flame widens and takes a slant-"M" shape. The side branches' thickness is reduced, and their luminosity is diminished. At the largest recess distance of $h_r = 6.75\,\mathrm{mm}$, the flame widens further, and the side branches are thinner and more inclined sideways. At this position, the flame retains an overall slanted "M" shape with two low-intensity lobes at the top of the side branches. When the atomizer is close to the injector outlet (for example, at $h_r = 2.75\,\mathrm{mm}$), there is a greater density of droplets near the axis (see Fig. 5). As a result, combustion occurs in the central area, leading to narrower flames with higher intensity. This is also observed in the LES calculations of the SICCA-Spray combustor in [25].

5. Measurements with flame modulation

The previous section described the behavior of SICCA-Spray under steady operating conditions. It is next logical to identify differences in the flame response through external acoustic modulation at the selected recess distances. This is done by first considering the flame images at different phase instants of the acoustic cycle, and it is then followed by the determination of the FDF.

5.1. *Flame images with acoustic modulation*

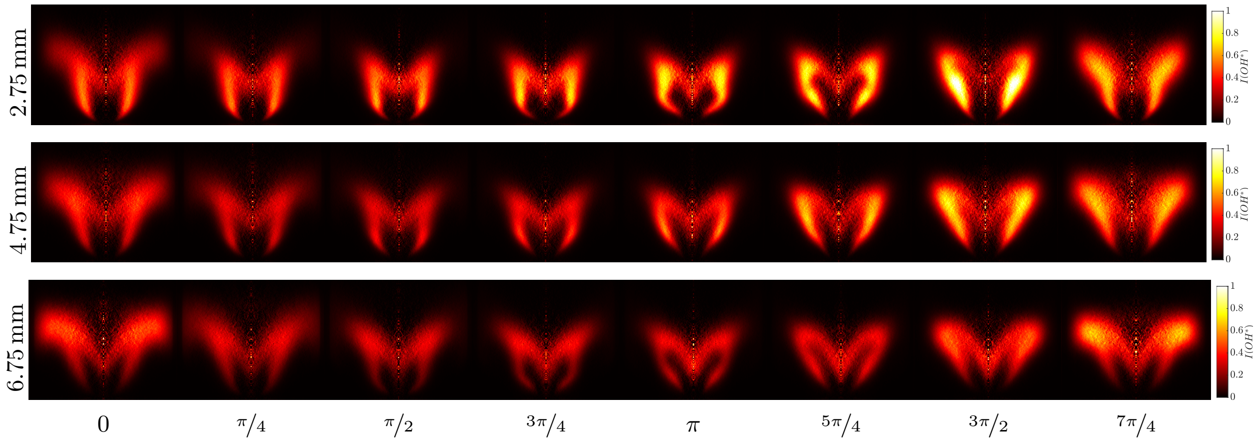

Figure 6: Flame images showing OH* chemiluminescence obtained when modulating the flame at $500\,\mathrm{Hz}$ with $u'_{c,r}/\overline{u}_{c,r} \approx 25\%$. An Abel deconvolution algorithm is applied to the images captured by the camera and displayed in false colors. The images are plotted at different phase instants of the wave generator signal φ_g, mentioned at the bottom.

Phase-averaged flame images are obtained using the ICCD camera fitted with an OH* filter when the flame is modulated at $500\,\mathrm{Hz}$ with an amplifier voltage of $3\,\mathrm{V}$, resulting in a velocity fluctuation level $u'_{c,r}/\overline{u}_{c,r} \approx 25\%$ at the injector outlet. Figure 6 shows the OH*-Abel inverted images at different phase instants of the wave generator signal φ_g. Overall, the flame size appears to be diminished between $\varphi_g = \pi/4$ to $\varphi_g = \pi$. Its size then increases, as observed for all the atomizer positions. However, the flame dynamics is altered with the recess values at any particular phase instant. The flames corresponding to h_r =$2.75\,\mathrm{mm}$ feature a “claw”-like shape near their anchor points at many phase instants. This feature is absent at $6.75\,\mathrm{mm}$ and is weakly present at a few phase instants for $4.75\,\mathrm{mm}$. On the other hand, the flame at $6.75\,\mathrm{mm}$ features wings at its top, which are absent at $2.75\,\mathrm{mm}$, but feebly present at some phase instants for $4.75\,\mathrm{mm}$. Thus, the flames at $4.75\,\mathrm{mm}$ possess the characteristics of those established at $2.75\,\mathrm{mm}$ and $6.75\,\mathrm{mm}$, which could not be previously identified in the steady flame images (discussed earlier in Section 4.4).

5.2. Flame describing functions (FDFs)

Flame describing functions are now commonly used to determine instability domains and interpret combustion dynamics phenomena. In configurations of the kind used in the present experiments, it is possible to define instability bands and use the FDF to see if a given operating point will be stable or unstable [35]. For this, it is important to locate the FDF phase function with respect to the instability bands in the frequency range corresponding to the acoustic modes of the system. The determination of the FDF raises issues that are discussed in what follows and also in Appendix A, where the FDF is determined in a way that notably differs from that used below, which relies on a determination of the relative heat release rate fluctuations (obtained from the chemiluminescence emission) and of the relative velocity disturbances that modulate the flame. As will be seen later, in Appendix A, the FDFs are obtained by measuring the velocity fluctuations upstream and downstream of the flame and compared with the FDFs obtained using chemiluminescence emission.

5.2.1. Heat release rate determination

Heat release rate fluctuations in spray flames of the kind considered in this investigation are mainly caused by velocity and equivalence ratio disturbances and may be expressed as:

$$\dot{Q}'/\overline{\dot{Q}} = \mathcal{F}_v(\dot{q}'_v/\overline{\dot{q}}_v) + \mathcal{F}_\phi(\phi'/\overline{\phi}) \tag{2}$$

where $\mathcal{F}_v$ and $\mathcal{F}_\phi$ represent describing functions with respect to relative volume flow rate and equivalence ratio fluctuations. As it is generally not easy to measure relative volume flow rate fluctuations, they are usually replaced by velocity fluctuations, as exemplified in [35] for the case of flames featuring nonuniform velocity distributions like those established by swirling injectors. It is shown that the axial velocity fluctuation is to be measured at a point designated by the subscript r such that $u'_{c,r}/\overline{u}_{c,r}$ coincides with the relative volume flow rate fluctuation $\dot{q}'_v/\overline{\dot{q}}_v$. For the swirler considered here, it was verified [35] that this equality is satisfied at a radius $r = 4\,\mathrm{mm}$ from the injector center and at a height $h = 2.5\,\mathrm{mm}$ above the chamber backplane. It is also ensured that, at this location, the droplet count is sufficient to retrieve the RMS velocity, and the fuel droplets are small enough to follow the flow with a negligible phase delay.

In principle, both $\mathcal{F}_v$ and $\mathcal{F}_\phi$ should be considered, but experiments with the present injectors indicate that the relative equivalence ratio fluctuations are weak compared to the relative velocity fluctuations. This is verified by complementing the steady OH* images shown in Fig. 4 (bottom row) with CH* chemiluminescence from the flame, the ratio between which is known to provide a measure of the equivalence ratio [38, 39]. The relative intensity deviation is obtained with the two chemiluminescence signals captured by the ICCD camera as,

$$I_{\text{rel}} = \Big[\frac{I^{x,z}_{CH^*}}{I^{x,z}_{OH^*}} - \frac{\overline{I^{x,z}_{CH^*}}}{\overline{I^{x,z}_{OH^*}}}\Big] / \Big[\frac{\overline{I^{x,z}_{CH^*}}}{\overline{I^{x,z}_{OH^*}}}\Big] \tag{3}$$

where $\overline{(.)}$ refers to the spatial averaging of a flame image. The captured images are first filtered to only retain portions that contain at least 20% of the maximum intensity. Figure 7 shows the spatially resolved relative intensity deviation under steady-state conditions at the three selected atomizer recess positions. It can be observed particularly from Fig. 7 (b) & (c) that the intensity deviation is only minor, mostly less than 5% in the flame zone. Although a slightly higher level of deviation is observed in certain regions close to the periphery, the data reliability is low here, owing to the

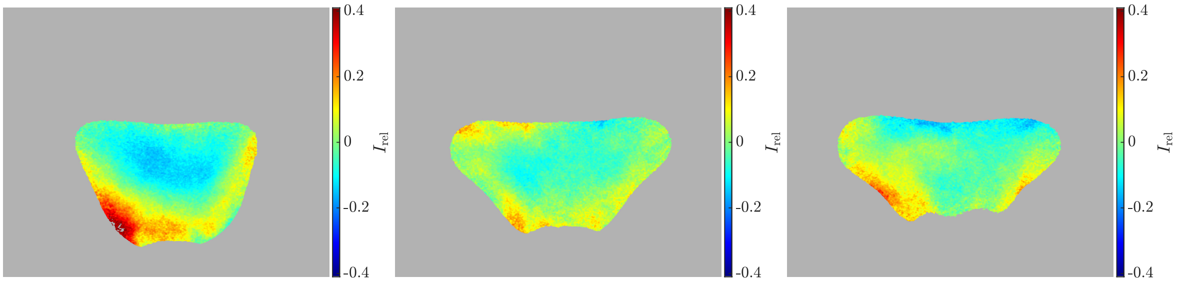

(a) $h_r = 2.75\,\mathrm{mm}$ (b) $h_r = 4.75\,\mathrm{mm}$ (c) $h_r = 6.75\,\mathrm{mm}$

Figure 7: Relative intensity deviation obtained using Eq. 3 at the three atomizer recess positions when the flame is stable.

reduced intensity signals in these regions. Thus, one can consider that the spatial equivalence ratio inhomogeneities in these spray flames are low at these two atomizer positions. However, one observes a higher level of relative intensity deviation at $h_r = 2.75\,\mathrm{mm}$ (Fig. 7 (a)), possibly indicating a spatial equivalence ratio variation in this particular case. The reason for the above observations can be attributed to the spray interaction with the walls of the terminal plate, as discussed in Section 4.2. When the atomizer is positioned further inside the injector (at $h_r = 4.75$ and $6.75\,\mathrm{mm}$), the part of the fuel spray that interacts with the converging cone and exits into the chamber is controlled by the air flow rate. This implies that the flow rate of the fuel spray that impacted this conical section directly depends on the air flow rate. Thus, when there is a pulsation of the air flow rate, the spray interacting with the wall fluctuates in phase. This appears to reduce the fluctuation in equivalence ratio compared to a case where the fuel is conveyed directly into the chamber without any impact (at $h_r = 2.75\,\mathrm{mm}$). Further, the presence of equivalence ratio fluctuations can be estimated when the flame is modulated at $500\,\mathrm{Hz}$ and the atomizer recess is at $h_r = 6.75\,\mathrm{mm}$. It is found that the fluctuation in equivalence ratio $\phi'/\overline{\phi}$ is only 4% as opposed to the velocity fluctuations $u'_{c,r}/\overline{u}_{c,r}$ at the injector exit, which is 22% (i.e., $\phi'/\overline{\phi} \ll u'_{c,r}/\overline{u}_{c,r}$). These results are shown in [37]. One may then assume, as a first approximation, that the term corresponding to equivalence ratio fluctuations in Eq. 2 may be neglected, link the relative heat release rate fluctuations to relative fluctuations in velocity, and only consider an FDF defined by the ratio of these two quantities:

$$\mathcal{F}_v(\omega, |u'_{c,r}/\overline{u}_{c,r}|) = (\dot{Q}'/\overline{\dot{Q}})/(u'_{c,r}/\overline{u}_{c,r}) \tag{4}$$

In the absence of equivalence ratio fluctuations, the light intensity fluctuations of the OH* radical $I'(OH^*)/\overline{I}(OH^*)$ are known to approximately represent the relative fluctuations in heat release rate $\dot{Q}'/\overline{\dot{Q}}$. This is thoroughly examined in [35] and discussed with further detail in [37] (Chapter 2) to confirm the applicability of chemiluminescence intensity approximately representing heat release fluctuations for these specific spray flames. In essence, we consider that the spray flames operate in a quasi-premixed mode with a recessed atomizer because of the spray-wall interaction, small droplet sizes, and high volatility of the heptane spray. Since this assumption may be questioned, we use an alternative technique in Appendix A to determine the FDF. This is based on the Rankine-Hugoniot (RH) condition and only requires the measurement of velocity fluctuations on the upstream and downstream sides of the flame. The resulting FDFs $\mathcal{F}_{RH}$ are compared with those determined using OH* chemiluminescence ($\mathcal{F}_v$), and it is found that the phase functions evolve in a similar fashion at all the three atomizer positions, whereas there are differences in the gain values with the gain of the RH method being generally lower than the gain deduced from chemiluminescence estimation of the heat release rate. It is noteworthy that the phase functions obtained with these independent methods are close and evolve in the same way so that they can be used with confidence in a stability analysis to predict potential instability, as explained later in this section. However, a possible error can be expected in the determination of growth rates due to the uncertainty in FDF gain.

5.2.2. FDFs at different atomizer positions

Figure 8 shows the FDFs in terms of gain G_F and phase φ_F at the three recess distances. Due to the difference in the flame shape shown in Fig. 4, one naturally expects that differences will be manifested in the FDFs as well.

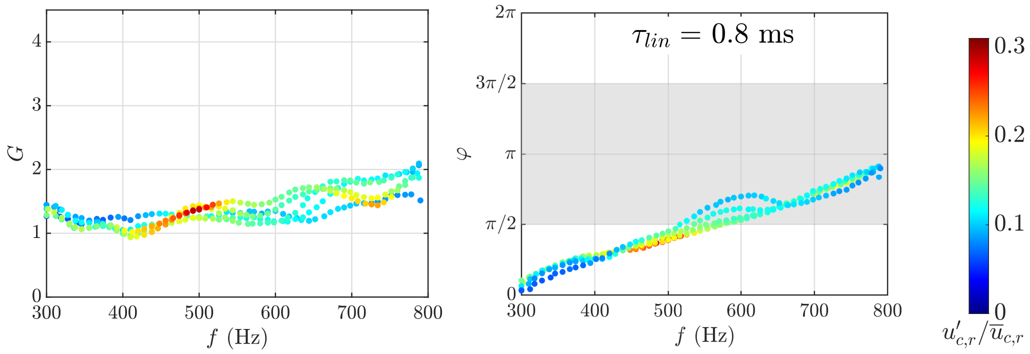

(a) $h_r = 2.75\,\mathrm{mm}$

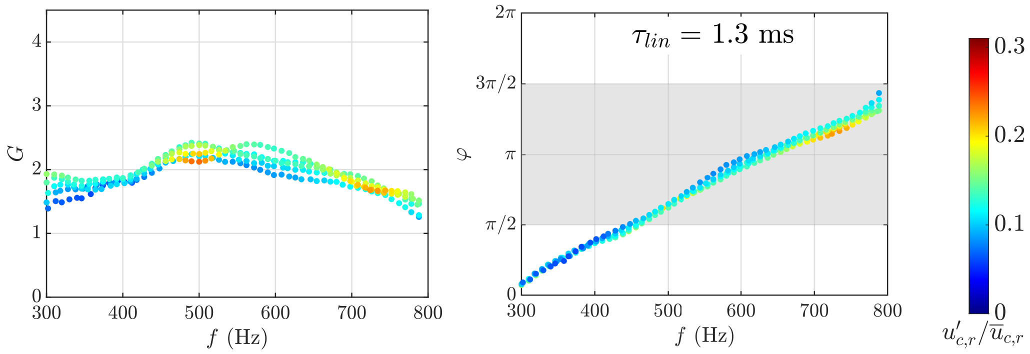

(b) $h_r = 4.75\,\mathrm{mm}$

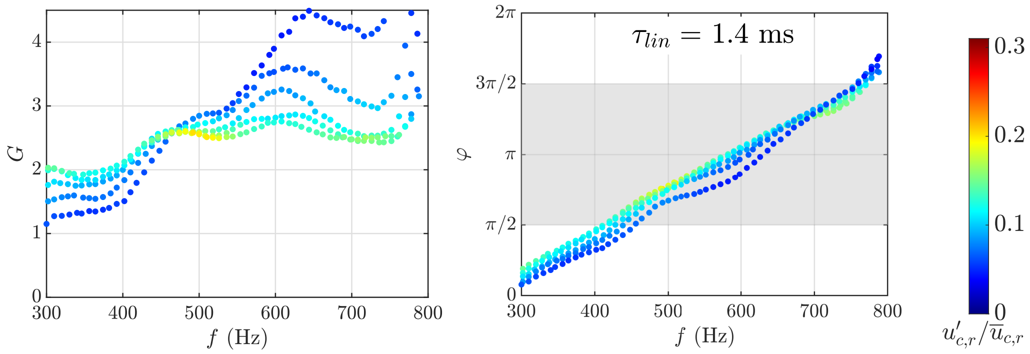

(c) $h_r = 6.75\,\mathrm{mm}$

Figure 8: Flame describing function gain G_F (top) and phase φ_F (bottom) for the three atomizer recess positions. The color scale represents the level of velocity fluctuations measured at a radius of $r = 4\,\mathrm{mm}$ and at a height of $h = 2.5\,\mathrm{mm}$ from the backplane. $u'_{c,r}$ and $\overline{u}_{c,r}$ are respectively the RMS and mean velocity. The gray bands indicate the approximate location of unstable bands deduced from the model proposed in [35]. The time delay τ_{lin} indicated on the phase plots is calculated by considering a linear evolution of the phase curve.

At $h_r = 2.75\,\mathrm{mm}$, the gain remains relatively flat until $600\,\mathrm{Hz}$, beyond which there is a moderate increase. The gain has a slightly higher value at $4.75\,\mathrm{mm}$ and takes the highest value when the atomizer is at $6.75\,\mathrm{mm}$. At this position, the gain notably depends on the fluctuation level. For the operating regimes considered here, there is almost no dependence of the phase on velocity fluctuation level, except close to $600\,\mathrm{Hz}$ for $2.75\,\mathrm{mm}$ and at low velocity fluctuation levels for $6.75\,\mathrm{mm}$. The phase curve slope changes at the various atomizer positions. By approximating a linear evolution, a time delay τ_{lin} can be calculated from the phase curves, and the corresponding values are indicated in Fig. 8. The delay is smallest at $2.75\,\mathrm{mm}$, while it takes larger values for the recess distances of $4.75\,\mathrm{mm}$ and $6.75\,\mathrm{mm}$. The difference in time delay at the various recess distances can be attributed to the difference in travel time between the injector outlet and the region where heat release is taking place, which may be approximated by the axial position of the heat release rate barycenter. This distance can be determined from the stable flame images shown in Section 4.4. The barycenter a_b calculated from these images takes the smallest value of $20.4\,\mathrm{mm}$ above the backplane at $h_r = 2.75\,\mathrm{mm}$. This can be expected as the flame appears visibly shorter at this recess location (see Fig. 4 bottom row). The barycenter distance takes values of $24.6\,\mathrm{mm}$ and $27.2\,\mathrm{mm}$ at $h_r = 4.75\,\mathrm{mm}$ and $6.75\,\mathrm{mm}$, respectively. Since the maximum mean axial velocity of air just above the injector outlet takes nearly the same values at the three atomizer positions (Section 4.1), one can expect the shortest time for the disturbances to reach the flame barycenter at the smallest recess distance.

5.2.3. Instability analysis with FDFs

The difference in the FDFs and their link to the SSO behavior can be interpreted by considering an instability analysis framework discussed in [35], where it is shown that for injectors that are weakly transparent to acoustic waves, it is preferable to represent their response by an impedance and in this way limit the analysis to the combustion chamber. It is then possible to define instability bands and examine the location of the phase function with respect to these bands ([35, 40]). This indicates whether a particular frequency corresponding to an eigenmode of the system falls within an unstable band. With similar injectors, it is shown in [35] that the unstable bands primarily depend on the phase of the impedance φ_ζ imposed by the injector at its outlet. The impedance itself should, in principle, be determined by modulating the system from downstream and measuring the injector response. Alternatively, it is possible to obtain impedance values by measuring the pressure and velocity fluctuations at the injector outlet when the system exhibits an SSO. This is achieved with chamber lengths $l_c = 365$ and $265\,\mathrm{mm}$, where the oscillations manifest at frequencies around $420\,\mathrm{Hz}$ and $600\,\mathrm{Hz}$, respectively. The measured impedances reported in Appendix B indicate that the impedance phase is $\varphi_\zeta \approx \pi$ at most frequencies corresponding to a phase opposition between pressure and axial velocity at the injector outlet. Considering this value for the impedance phase and using the model described in [35], one finds that the unstable band is located between $\pi/2$ to $3\pi/2$ (mod 2π). The first of these bands is superimposed on the phase curves in Fig. 8. At $h_r = 2.75\,\mathrm{mm}$, the phase curve enters the unstable band around $580\,\mathrm{Hz}$ when the velocity fluctuation level is highest. The instability frequency reported in Section 3 at this atomizer position is below $590\,\mathrm{Hz}$ at $l_c = 365$ and $265\,\mathrm{mm}$, which is just at the lower limit of the unstable band. This explains why the system is marginally unstable observed at this atomizer position. However, at $l_c = 215\,\mathrm{mm}$, the instability frequency is above $600\,\mathrm{Hz}$ (see Fig. 2 (b) bottom row), and the FDF phase curves at $h_r = 2.75\,\mathrm{mm}$ now fall inside the unstable band (Fig. 8 (a) right) indicating that a self-sustained instability is possible in this case. At $h_r = 4.75$ and $6.75\,\mathrm{mm}$, the phase curves cross the unstable band at a lower frequency ($\approx 400\,\mathrm{Hz}$), indicating that a system having an acoustic mode at frequencies higher than $400\,\mathrm{Hz}$ and lower than 750–800 Hz may develop a self-sustained oscillation, provided that the gain is sufficiently high, which is the case at these two atomizer positions (Fig. 8 (b) & (c)). This corresponds to what is observed during the SSOs reported in Section 3 (Fig. 2), where the instabilities occur around $556\,\mathrm{Hz}$ and $430\,\mathrm{Hz}$ at $l_c = 265\,\mathrm{mm}$ and $365\,\mathrm{mm}$ respectively at $h_r = 4.75\,\mathrm{mm}$, and around $530\,\mathrm{Hz}$ and $410\,\mathrm{Hz}$ at $l_c = 265\,\mathrm{mm}$ and $365\,\mathrm{mm}$, respectively at $h_r = 6.75\,\mathrm{mm}$.

The previous analysis retrieves many of the features observed experimentally particularly at the two longer chamber lengths of 265 and $365\,\mathrm{mm}$ for the three recess positions. However, this analysis does not explain the nearly-stable behavior prevailing for the largest recess distance and for a chamber length $l_c = 215\,\mathrm{mm}$ (see the third row and first column of Fig. 2). As pointed out in [35], the unstable band location may change with the frequency and may also depend on the amplitude of oscillation for a particular injector. The lower boundary of the first band could be as low as $\pi/4$, in which case, the upper limit would be close to $5\pi/4$. In the higher frequency range, the unstable band is perhaps displaced to these lower phase values, and the unstable range where the phase curve would cross the unstable band might not coincide with the frequency of oscillation corresponding to the chamber 1L (first longitudinal) mode, eventually resulting in a stable operation at the largest atomizer recess distances. In addition, being inside the unstable band is only necessary but not a sufficient condition for instability. One can be inside the unstable band but still not witness any instability if the gain is not large enough to overcome the damping rate or if the damping rate itself is very high. Although this may not be the case here, considering the high gain values at the instability frequencies of $l_c = 215\,\mathrm{mm}$, this is still worth noting.

6. Conclusions

This article describes the effect of spray dynamics on combustion instabilities through experiments carried out on a single swirl injector combustor fueled by a liquid-heptane pressure atomizer. By varying the fuel atomizer position in the axial direction, one observes three distinct instability zones, characterized by jumps in amplitude and frequency at two of the chamber lengths tested. The amplitude of instability decreases when the atomizer recess is diminished, indicating that the system can be stabilized by moving the atomizer towards the injector outlet. However, these observations are reversed at a chamber length corresponding to higher eigenfrequencies where the instability is only marginal and the amplitude increases when the atomizer recess is diminished. It is first found from light scattering images that the spray interaction with the injector end piece plays a key role. When the atomizer is recessed deep inside the injector, the spray impinges on this component, whereas this process is reduced when the atomizer is closer to the outlet, thus modifying the spatial dispersion and possibly the convection time of the fuel droplets. It is next found that this modifies the flame shape and dynamics. This is further reflected as changes in the flame describing function (FDF), determined by two independent measurement techniques in this work. It is then shown that the FDF data, in combination with a model, can be used to explain most of the experimental observations. A smaller recess distance results in a lower gain and a shorter delay. When the recess distance is increased, the delay is enhanced, and the FDF phase may fall within a band of instability for certain frequency ranges that match one of the system's eigenmodes. At the same time, the gain may take values that are sufficiently large to induce an unstable oscillation. The present data indicate that small changes in the injector geometry can substantially impact the system dynamics and change the operating regime. This study, therefore, constitutes an interesting test case in the development of instability prediction tools and may also help devise control techniques for instability suppression.

Acknowledgments

This work was supported by the European Union's Horizon 2020 research and innovation programme Annulight, with grant agreement no. 765998.

Appendix A. Alternative determination of the flame describing function

The flame describing functions are often determined by assuming that the relative heat release rate fluctuations that appear in their numerators can be deduced from chemiluminescence intensity measurements like that of OH*, as exemplified in Section 5.2. This is generally acceptable when the flame is formed by fully premixed reactants. This procedure is more questionable in the case of spray flames. It is shown, however, that this is justified if the flames operate in an approximately premixed mode, as shown in the main text. But it is also worth exploring an alternative method for determining the FDF that relies on the Rankine-Hugoniot (RH) condition across the flame and only involves velocity measurements on its upstream and downstream sides. The RH jump condition across the flame links the velocity perturbations on the upstream and downstream sides of the flame to the heat release rate fluctuations as:

$$S_2 u_3' - S_2 u_2' = \frac{\gamma - 1}{\rho_0 c_0^2} \dot{Q}' \tag{A.1}$$

where S_2 is the cross-sectional area at the flame section, u_3' and u_2' are the velocity fluctuations before and after the flame, and $\dot{Q}'$ designates the heat release rate fluctuations. A schematic representation of an idealized injector and combustion chamber section of the present system is shown in Fig. A.9, depicting these various components. It is convenient to express the heat release rate fluctuations in the flame in terms of the FDF $\mathcal{F}_{RH}$ and of velocity

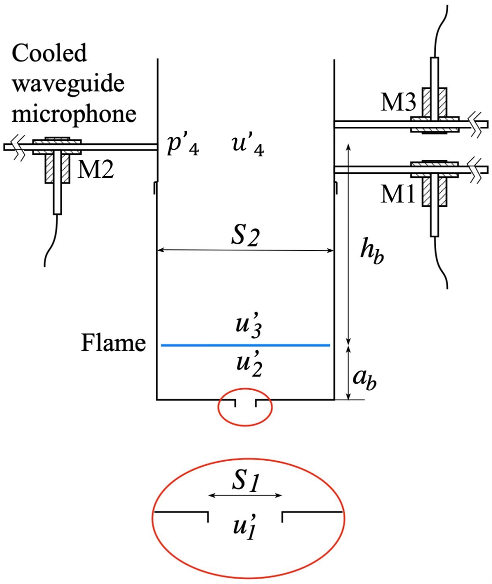

Figure A.9: A schematic representation of the injector and combustion chamber showing the locations of the three chamber microphones.

fluctuations at a point '$\{c,r\}$' close to the injector exit, where relative velocity fluctuations match the relative volume flow rate fluctuations. One may then write

$$\dot{Q}' = \overline{\dot{Q}}\mathcal{F}_{RH}\frac{u'_{c,r}}{\overline{u}_{c,r}} \tag{A.2}$$

where $\overline{u}_{c,r}$ and $u'_{c,r}$ are respectively the measured mean and fluctuation velocity at the nominal FDF measurement location. The subscript RH is added to the FDF notation to distinguish it from the FDF $\mathcal{F}_v$ in the main text that is determined using OH* chemiluminescence. It is also convenient to express the mean heat release rate $\overline{\dot{Q}} = \dot{m}\overline{c_p}(T_3 - T_2)$, where $\dot{m} = \rho_1 S_1 \overline{u}_1$, $\overline{u}_1$ is the bulk velocity at the injector exit, and S_1 is the area of the injector exit section, T_2 and T_3 designate the temperatures before and after the flame, and $\overline{c_p}$ is a mean specific heat such that $\overline{c_p} = \frac{1}{T_3-T_2}\int_{T_2}^{T_3} c_p dT = \frac{\dot{m}_f}{\dot{m}}\frac{\Delta h}{T_3-T_2}$, where Δh is the lower calorific value and $\dot{m}_f$ is the fuel mass flow rate. After substituting the above expressions in Eq. A.1, the jump condition becomes

$$S_2 u'_3 - S_2 u'_2 = \Xi\Gamma\Theta S_1 \mathcal{F}_{RH} u'_{c,r} \tag{A.3}$$

Here $\Xi = \overline{u}_1/\overline{u}_{c,r}$, $\Theta = T_3/T_2 - 1$ is the volumetric expansion parameter across the flame and $\Gamma = \overline{c_p}/c_p$. $\overline{u}_1$ is the bulk velocity at section S_1, which is different from the mean velocity $\overline{u}_{c,r}$ measured at a radius r from the injector axis and height h above the backplane. The volume flow rate fluctuation at the injector exit is $\dot{q}'_v = S_2 u'_2$, assuming the volumetric flow rate fluctuation on the upstream side of the flame is conserved. As the measured relative velocity fluctuations at injector exit equals the volume flow rate fluctuation, i.e., $\dot{q}'_v/\overline{\dot{q}}_v = u'_{c,r}/\overline{u}_{c,r}$, one can write $S_1\overline{u}_1 u'_{c,r}/\overline{u}_{c,r} = S_2 u'_2$ or $S_1 \Xi u'_{c,r} = S_2 u'_2$. Using this expression, Eq. A.3 can be cast in the simple form:

$$S_2 u'_3 - S_1 \Xi u'_{c,r} = S_1 \Xi\Gamma\Theta\mathcal{F}_{RH} u'_{c,r} \tag{A.4}$$

The flame describing function $\mathcal{F}$ is then given by

$$\mathcal{F}_{RH} = \frac{1}{\Xi\Gamma\Theta}\left[\frac{S_2}{S_1}\frac{u'_3}{u'_{c,r}} - \Xi\right] \tag{A.5}$$

The flame describing function may be determined from the velocities upstream ($u'_{c,r}$) and downstream (u'_3) of the

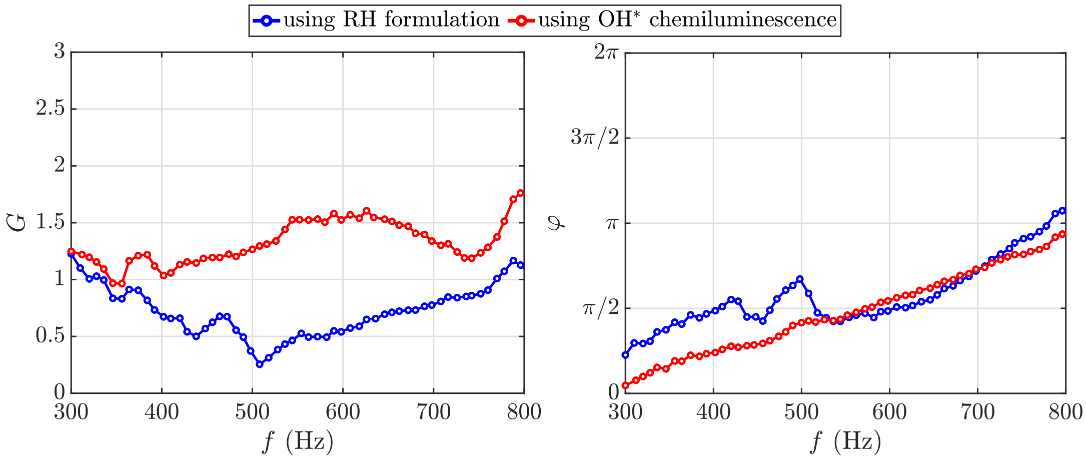

(a) $h_r = 2.75\,\mathrm{mm}$

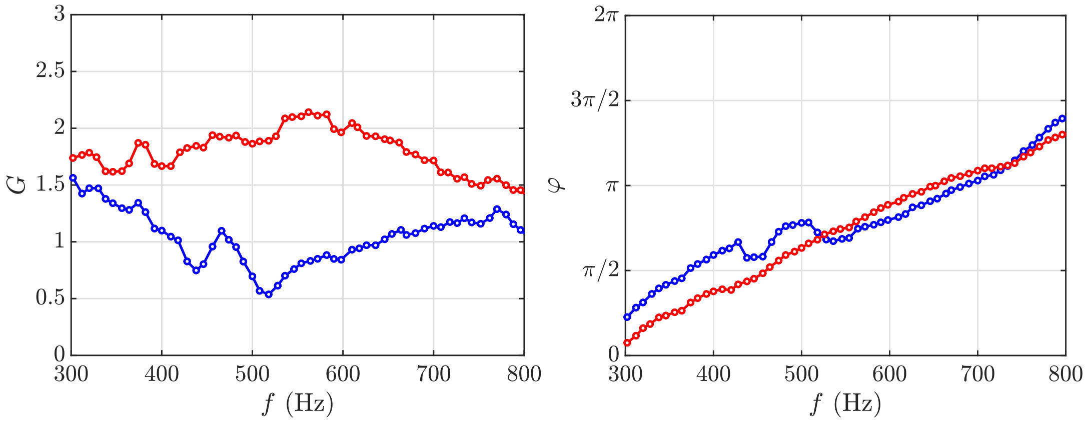

(b) $h_r = 4.75\,\mathrm{mm}$

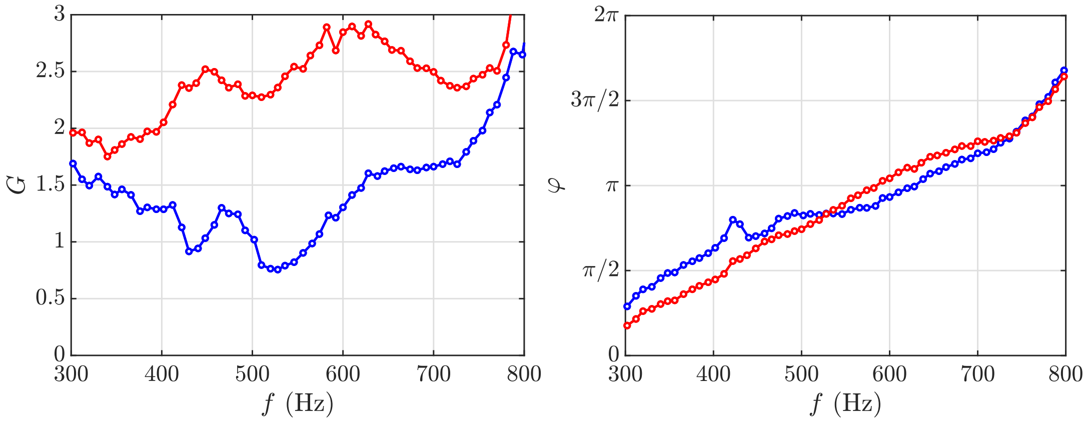

(c) $h_r = 6.75\,\mathrm{mm}$

Figure A.10: Comparison of flame describing function determined from first principles using Rankine-Hugoniot formulation and using OH* chemiluminescence. The results are shown at three recess distances when modulating the flow at maximum possible amplifier voltage to ensure the best signal-to-noise acquisition.

flame without the need for measuring the heat release rate fluctuations. Here, the upstream velocity $u'_{c,r}$ is obtained through LDA as described earlier in this article. The downstream velocity fluctuation is deduced from the pressure fluctuations detected by three microphones, M_1, M_2 and M_3 (shown in Fig. A.9), mounted on waveguides and plugged onto the downstream side of the flame. The velocity u'_4 determined from the microphone signals corresponds to section 4, where the central microphone M_2 is located. This section is at a distance h_b from the flame, and it is necessary to link sections 3 and 4 by considering acoustic propagation in a constant area channel. This is conveniently achieved by using the transfer matrix between these two sections

$$\begin{bmatrix} p'_3/\rho_c c_c \\ u'_3 \end{bmatrix} = \begin{bmatrix} \cos k_c h_b & -i \sin k_c h_b \\ -i \sin k_c h_b & \cos k_c h_b \end{bmatrix} \begin{bmatrix} p'_4/\rho_c c_c \\ u'_4 \end{bmatrix} \tag{A.6}$$

where k_c is the wavenumber in the hot gases and h_b represents the distance between the flame barycenter and section 4, where the downstream velocity is being measured. One may then obtain an expression for $\mathcal{F}_{RH}$ as

$$\mathcal{F}_{RH} = \frac{1}{\Gamma\Theta} \left[\frac{1}{\Xi} \frac{S_2}{S_1} \frac{u'_4}{u'_{c,r}} \cos k_c h_b - i \frac{1}{\Xi} \frac{S_2}{S_1} \sin k_c h_b \frac{p'_4}{\rho_c c_c u'_{c,r}} - 1 \right] \tag{A.7}$$

It is instructive to compare the FDF estimates determined from the chemiluminescence method with the FDF determined using RH formulation (Eq. A.7) to see if the latter method yields results that are compatible with those obtained from the more standard method.

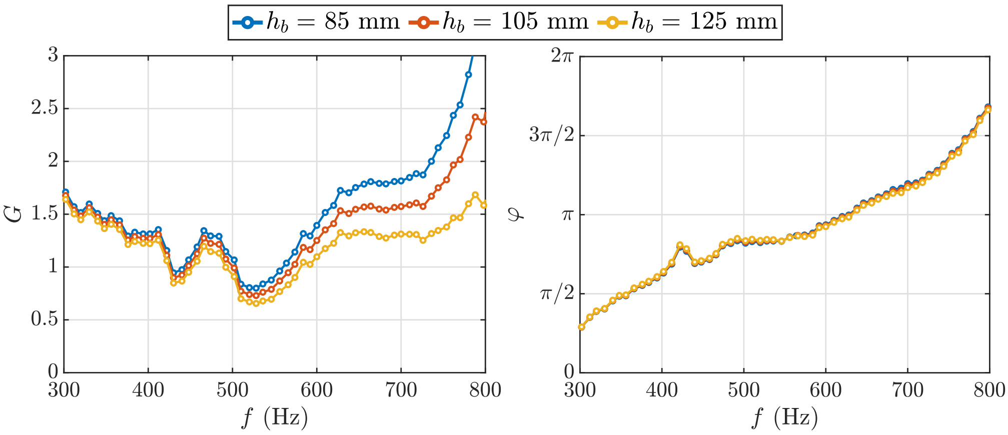

Figure A.11: Sensitivity of flame describing function determined using RH formulation to the distance h_b between the flame and measurement location at $h_r = 6.75\,\mathrm{mm}$.

For the FDF determination using Eq. A.7, one has to provide the temperature T_c in the chamber to calculate the density ρ_c, speed of sound c_c and wavenumber k_c. The temperature is estimated using an R-type thermocouple placed in the section corresponding to microphone M_2. Figure A.10 shows the FDF gain and phase obtained with the two methods at the various atomizer positions and at the maximum amplifier voltage supplied to the driver units to optimize the signal-to-noise ratio. One observes that the phase evolution corresponding to the two methods generally agree, particularly beyond 500 Hz, and that this holds for the three atomizer locations. This match indicates that the FDF determined using the OH* chemiluminescence provides phase functions that may be used with some confidence in instability prediction schemes like that used in this article. A minor difference, however, exists at frequencies below 500 Hz at $h_r = 2.75\,\mathrm{mm}$, and this might perhaps be due to the presence of equivalence ratio fluctuations at this atomizer location, as discussed in Section 5.2. Although the gain values have the same order of magnitude, there are non-negligible differences between the two methods. A similar observation on a mismatch in gain between the FDF determined by purely acoustic method and optical method considering OH* chemiluminescence was reported by [41, 42], but one cannot say at this point which of the two methods gives rise to this error.

One possible reason for the gain mismatch could be in the determination of chamber temperature T_c. Although this is measured using an R-type thermocouple close to the measurement section of the chamber microphones, a

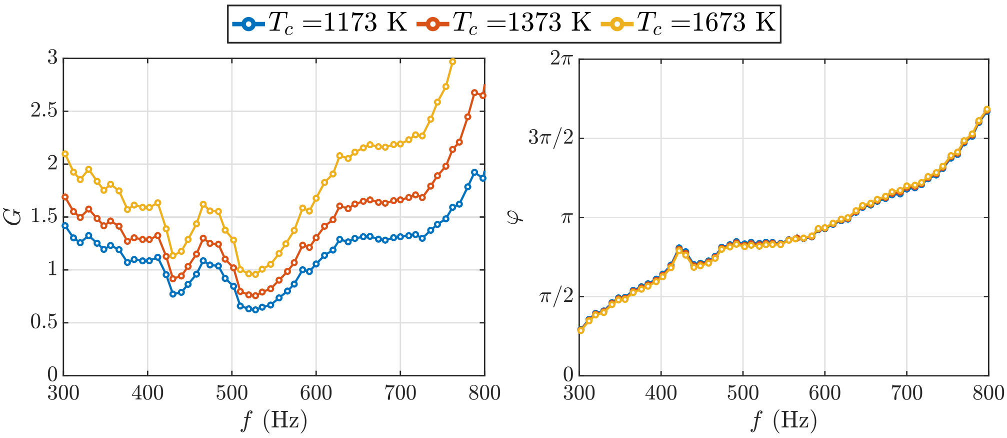

Figure A.12: Sensitivity of flame describing function determined using RH formulation to the temperature T_c in the chamber at $h_r = 6.75\,\mathrm{mm}$.

temperature gradient exists in the chamber and considering a single value might not be suitable. The other cause for this mismatch can be in the value of h_b, which represents the distance between the flame barycenter and the location where velocity is extracted from the microphone signals. One does not know if this location for the flame is exact. A sensitivity analysis is thus carried out to establish the FDF dependence on these two parameters. Results displayed in Fig. A.11 and A.12 indicate that the phase determined using the RH method remains nearly the same, but the FDF gain is found to be sensitive to both h_b and T_c. A $20\,\mathrm{mm}$ deviation in the exact location of the flame with respect to the measurement section can result in a 20% variation in the FDF gain, especially in the higher frequency range (beyond $600\,\mathrm{Hz}$—see Fig. A.11). The influence of chamber temperature is seen to have a stronger influence on the FDF gain, and a difference of $200\,\mathrm{K}$ can approximately result in a 30% deviation in the FDF gain (see Fig. A.12). A precise determination of these parameters is not easy, indicating that the method based on the RH condition is not as reliable as may seem at first sight. This method also raises some practical difficulties. One issue is that the chamber must be much longer than the flame to mount the downstream microphones and ensure sufficient spacing between them. The longer chamber raises risk of encountering self-sustained oscillations, which would then hinder obtaining the flame describing function, as these must be obtained by modulating a stable flame [33]. This problem can be avoided when performing chemiluminescence measurements, as this only requires a chamber length sufficient enough to enclose the flame. Further measurements and analysis are required to assess the suitability of using the FDF gain determined using RH formulation and are beyond the scope of the present work. One may, however, retain that the phase function obtained with the two methods are in agreement and use one or the other in the stability analysis and data interpretation.

Appendix B. Impedance at the injector outlet during self-sustained oscillations

As indicated earlier in Section 5.2, the injector impedance is measured when the system features limit cycle self-sustained oscillations at $l_c = 265\,\mathrm{mm}$ and $365\,\mathrm{mm}$. However, the measurements at $h_r = 2.75\,\mathrm{mm}$ are slightly less reliable as the system only exhibits marginal instability in these cases. Figure A.13 shows the impedance modulus G_ζ and phase φ_ζ measured at the injector outlet. The highest frequency at each chamber length corresponds to the lowest atomizer recess distance and so on. One may refer to Fig. 2 for the relation between oscillation frequency and recess distance. The impedance phase decides the position of the unstable band and is mostly close to π in the frequency range considered except below $440\,\mathrm{Hz}$, where the phase is rather close to $\pi/2$. Nevertheless, in the simple analysis using FDFs described in Section 5.2, an impedance phase of π is considered to interpret the SSO behavior. The modulus of impedance is approximately equal to 0.5 in the frequency range considered.

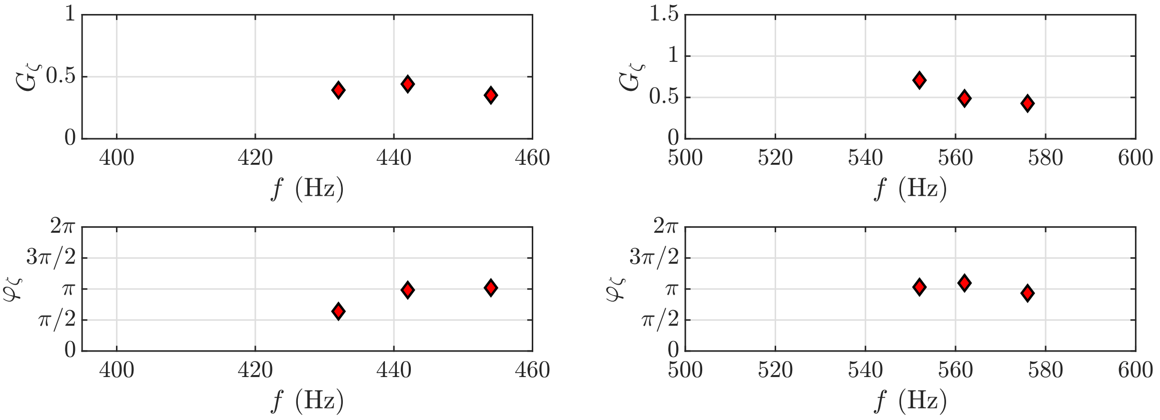

(a) $l_c = 365\,\mathrm{mm}$

(b) $l_c = 265\,\mathrm{mm}$

Figure A.13: The modulus G_ζ and phase φ_ζ of the injector impedance measured in SICCA-Spray at $l_c = 365$ and $265\,\mathrm{mm}$, and at frequencies corresponding to the three atomizer positions of $h_r = 2.75$, 4.75, and $6.75\,\mathrm{mm}$. The highest frequency at each chamber length corresponds to the lowest recess distance and so on.

References

[1] T. C. Lieuwen, V. Yang (Eds.), Combustion instabilities in gas turbine engines: operational experience, fundamental mechanisms, and modeling, Vol. 210, Am. Inst. Aeronaut. Astronaut., 2005.

[2] T. Poinsot, Prediction and control of combustion instabilities in real engines, Proc. Combust. Inst. 36 (2017) 1–28.

[3] M. Mazur, Y. H. Kwah, T. Indlekofer, J. R. Dawson, N. A. Worth, Self-excited longitudinal and azimuthal modes in a pressurised annular combustor, Proc. Combust. Inst. 38 (2021) 5997–6004.

[4] K. Prieur, D. Durox, S. Schuller, S. Candel, Strong azimuthal combustion instabilities in a spray annular chamber with intermittent partial blow-off, J. Eng. Gas Turb. Power 140 (2018) 031503.

[5] G. Vignat, D. Durox, A. Renaud, S. Candel, High amplitude combustion instabilities in an annular combustor inducing pressure field deformation and flame blow off, J. Eng. Gas Turb. Power 142 (2020) 011016.

[6] P. Wolf, G. Staffelbach, L. Y. M. Gicquel, J.-D. Müller, T. Poinsot, Acoustic and large eddy simulation studies of azimuthal modes in annular combustion chambers, Combust. Flame 159 (2012) 3398–3413.

[7] R. Bhatia, W. A. Sirignano, One-dimensional analysis of liquid-fueled combustion instability, J. Propul. Power 7 (1991) 953–961.

[8] W. A. Sirignano, J. P. Delplanque, C. H. Chiang, R. Bhatia, Liquid-propellant droplet vaporization: A rate-controlling process for combustion instability, in: V. Yang, W.E. Anderson (Eds.), Liquid Rocket Engine Combustion Instability, Vol. 169, Am. Inst. Aeronaut. Astronaut., 1995.

[9] T. Yi, D. A. Santavicca, Combustion instability and flame structure of turbulent swirl-stabilized liquid-fueled combustion, J. Propul. Power 28 (2012) 1000–1014.

[10] W. A. Sirignano, Driving mechanisms for combustion instability, Combust. Sci. Tech. 187 (2015) 162–205.

[11] P. Rajendram Soundararajan, G. Vignat, D. Durox, A. Renaud, S. Candel, Effect of different fuels on combustion instabilities in an annular combustor, J. Eng. Gas Turb. Power 143 (2021) 031007.

[12] F. Giuliani, P. Gajan, O. Diers, M. Ledoux, Influence of pulsed entries on a spray generated by an air-blast injection device: An experimental analysis on combustion instability processes in aeroengines, Proc. Combust. Inst. 29 (2002) 91–98.

[13] X. Yang, A. Turan, Simulation of liquid jet atomization coupled with forced perturbation, Phys. Fluids 29 (2017) 022103.

[14] R. I. Sujith, An experimental investigation of interaction of sprays with acoustic fields, Exp. Fluids 38 (2005) 576–587.

[15] R. I. Sujith, G. A. Waldherr, J. I. Jagoda, B. T. Zinn, Experimental investigation of the evaporation of droplets in axial acoustic fields, J. Propul. Power 16 (2000) 278–285.

[16] C. Pera, J. Reveillon, Direct numerical simulation of spray flame/acoustic interactions, Proc. Combust. Inst. 31 (2007) 2283–2290.

[17] J. B. Greenberg, D. Katoshevski, Spray flame dynamics with oscillating flow and droplet grouping, Combust. Theory Model. 16 (2012) 321–340.

[18] J. Eckstein, E. Freitag, C. Hirsch, T. Sattelmayer, Experimental study on the role of entropy waves in low-frequency oscillations in a RQL combustor, J. Eng. Gas Turb. Power 128 (2006) 264–270.

[19] J. M. Apeloig, F.-X. d'Herbigny, F. Simon, P. Gajan, M. Orain, S. Roux, Liquid-fuel behavior in an aeronautical injector submitted to thermoacoustic instabilities, J. Propul. Power 31 (2015) 309–319.

[20] E. Lo Schiavo, D. Laera, E. Riber, L. Gicquel, T. Poinsot, Effects of liquid fuel/wall interaction on thermoacoustic instabilities in swirling spray flames, Combust. Flame 219 (2020) 86–101.

[21] M. Zhu, A. P. Dowling, K. N. C. Bray, Combustion oscillations in burners with fuel spray atomisers, Turbo Expo: Power for Land, Sea, and Air 78590 (1999) paper V002T02A057.

[22] M. de la Cruz García, E. Mastorakos, A. P. Dowling, Investigations on the self-excited oscillations in a kerosene spray flame, Combust. Flame 156 (2009) 374–384.

[23] S. Tachibana, K. Saito, T. Yamamoto, M. Makida, T. Kitano, R. Kurose, Experimental and numerical investigation of thermo-acoustic instability in a liquid-fuel aero-engine combustor at elevated pressure: Validity of large-eddy simulation of spray combustion, Combust. Flame 162 (2015) 2621–2637.

[24] A. Innocenti, A. Andreini, B. Facchini, A. Peschiulli, Numerical analysis of the dynamic flame response of a spray flame for aero-engine applications, Intl. J. Spray Combust. Dyn. 9 (2017) 310–329.

[25] E. Lo Schiavo, D. Laera, E. Riber, L. Gicquel, T. Poinsot, On the impact of fuel injection angle in Euler–Lagrange large eddy simulations of swirling spray flames exhibiting thermoacoustic instabilities, Combust. Flame 227 (2021) 359–370.

[26] M. P. Juniper, S. M. Candel, The stability of ducted compound flows and consequences for the geometry of coaxial injectors, J. Fluid Mech. 482 (2003) 257–269.

[27] L. Zhang, Y. Li, X. Wang, V. Yang, Effect of recess length on flow dynamics in gas-centered liquid-swirl coaxial injectors under supercritical conditions, Aerospace Sci. Tech. (2022) 107757.

[28] J. F. Z. Usandivaras, A. Urbano, M. Bauerheim, B. Cuenot, Large eddy simulations and deep learning for the investigation of recess variation of a shear-coaxial injector, Space Propul. Conf. (2022) paper no. 246.

[29] D. L. Straub, G. A. Richards, Effect of fuel nozzle configuration on premix combustion dynamics, Turbo Expo: Power for Land, Sea, and Air (1998) paper 98–GT–492.

[30] J.-Y. Lee, E. Lubarsky, B. T. Zinn, "Slow" active control of combustion instabilities by modification of liquid fuel spray properties, Proc. Combust. Inst. 30 (2005) 1757–1764.

[31] G. Vignat, P. Rajendram Soundararajan, D. Durox, A. Vié, A. Renaud, S. Candel, A joint experimental and les characterization of the liquid fuel spray in a swirl injector, J. Eng. Gas Turb. Power 143 (2021) 081019.

[32] K. Prieur, D. Durox, J. Beaunier, T. Schuller, S. Candel, Ignition dynamics in an annular combustor for liquid spray and premixed gaseous injection, Proc. Combust. Inst. 36 (2017) 3717–3724.

[33] P. Rajendram Soundararajan, G. Vignat, D. Durox, A. Renaud, S. Candel, Do flame describing functions suitably represent combustion dynamics under self-sustained oscillations?, J. Sound Vib. 534 (2022) 117034.

[34] A. F. Seybert, D. F. Ross, Experimental determination of acoustic properties using a two-microphone random-excitation technique, J. Acoust. Soc. Am. 61 (1977) 1362–1370.

[35] P. Rajendram Soundararajan, D. Durox, A. Renaud, G. Vignat, S. Candel, Swirler effects on combustion instabilities analyzed with measured FDFs, injector impedances and damping rates, Combust. Flame 238 (2022) 111947.

[36] G. Vignat, D. Durox, S. Candel, The suitability of different swirl number definitions for describing swirl flows: Accurate, common and (over-) simplified formulations, Prog. Energy Combust. Sci. 89 (2022) 100969.

[37] P. Rajendram Soundararajan, Investigation of combustion instabilities in annular combustors combining injector dynamics and flame describing functions determined in simplified configurations, Ph.D. thesis, Université Paris-Saclay (2022). `doi:https://hal.archives-ouvertes.fr/tel-03741349`.

[38] M. Orain, Y. Hardalupas, Effect of fuel type on equivalence ratio measurements using chemiluminescence in premixed flames, C. R. Mécanique 338 (2010) 241–254.

[39] Y. Ding, D. Durox, N. Darabiha, T. Schuller, Combustion state monitoring of premixed heating appliances with flame ionization current and chemiluminescence, Combust. Sci. Technol. 191 (2019) 382–401.

[40] T. Schuller, T. Poinsot, S. Candel, Dynamics and control of premixed combustion systems based on flame transfer and describing functions, J. Fluid Mech. 894.

[41] B. Schuermans, F. Guethe, W. Mohr, Optical transfer function measurements for technically premixed flames, J. Eng. Gas Turb. Power 132.

[42] R. Gaudron, M. Gatti, C. Mirat, T. Schuller, Impact of the acoustic forcing level on the transfer matrix of a turbulent swirling combustor with and without flame, Flow, Turbul. Combust. 103 (2019) 751–771.